



Hierarchical and ultrathin copper nanosheets synthesized via galvanic replacement for selective electrocatalytic carbon dioxide conversion to carbon monoxide



Jing Pan^{a,b}, Yuanmiao Sun^c, Peiling Deng^a, Fan Yang^a, Shenghua Chen^a, Qitao Zhou^d,
Ho Seok Park^{b,*}, Hongfang Liu^a, Bao Yu Xia^{a,*}

^a Key Laboratory of Material Chemistry for Energy Conversion and Storage (Ministry of Education), Hubei Key Laboratory of Material Chemistry and Service Failure, School of Chemistry and Chemical Engineering, Wuhan National Laboratory for Optoelectronics, Huazhong University of Science and Technology (HUST), 1037 Luoyu Road, Wuhan 430074, PR China

^b School of Chemical Engineering, Sungkyunkwan University, 2066 Seobu-ro, Jangan-gu, Suwon-si, Gyeonggi-do, 440-746, Republic of Korea

^c School of Materials Science and Engineering, Nanyang Technological University, Singapore 639798, Singapore

^d Creative Research Initiative Center for Functionally Antagonistic Nano-Engineering Department of Mechanical Engineering, Korea Advanced Institute of Science and Technology (KAIST), 291 Daehak-ro, Yuseong-gu, Daejeon 34141, Republic of Korea

ARTICLE INFO

Keywords:

Metal nanosheets
CO₂ conversion
Electrocatalyst
Hierarchical structure
DFT calculation

ABSTRACT

Electrochemical conversion of carbon dioxide (CO₂) to desirable products with high selectivity and efficiency remains critical challenges in balancing carbon cycle for sustainable society. Herein, we demonstrate the hierarchical porous architectures assembled by ultrathin copper (Cu) nanosheets (NS) via a simple galvanic replacement method for the improved selectivity of CO₂ conversion with a large current density. Specifically, the optimized hierarchical Cu electrodes achieve high selectivity and activity to convert CO₂ into CO, showing a Faradaic efficiency (FE) of 74.1%, record-high partial current density of 23.0 mA cm⁻², and turnover frequency of 0.092 s⁻¹ for CO product as well as FE of 24.8% for H₂ at potential of -1.0 V vs RHE. The onset potential for the CO₂ conversion is -0.29 V vs RHE. Theoretical calculations indicate that the abundant vacancy defects exposed on ultrathin Cu nanosheets can accelerate the initial kinetics of CO formation during the CO₂ conversion process. As demonstrated by experimental and computational analyses, the unique hierarchical architecture of integrated Cu electrode contributes the outstanding electrocatalytic performance due to the rapid mass and electrons transport as well as the abundant active sites and associated intrinsic activity.

1. Introduction

Electrocatalytic conversion of carbon dioxide (CO₂) into valuable chemicals is considered as a promising and ultimate solution to resolve the problem of excess CO₂ emission for the sustainable ecological system [1]. Among various products derived from CO₂ conversion, carbon monoxide (CO) is readily applied into marketing and can also mix with hydrogen (H₂) to form syngas, a crucial chemical of Fischer-Tropsch (FT) reaction to produce liquid fuels [2]. Thus, a vital target for CO₂ electrolysis is to simultaneously obtain CO product with high selectivity and yield. However, it is difficult to achieve high yield of CO using the existing electrocatalysts [3].

Recently, two-dimensional (2D) metal nanomaterials have acknowledged significant courtesy owing to their unique surface chemistry for electrocatalytic applications [4]. In a sharp contrast to bulk

counterpart, 2D metal nanomaterials exhibit much higher catalytic activities as their structures are well defined with the increased numbers of surface active sites and/or improved intrinsic activity [5]. Important examples including few-layered Sb [6], Co [7], and Sn [8] nanosheets demonstrate the enhanced product selectivity for electrochemical CO₂ conversion. Nevertheless, the synthetic methods of metal nanosheets are usually too complicated and time consuming for practical applications [9]. Moreover, It is difficult for the formation of 2D metallic nanostructure with low stacking fault energies or huge elastic anisotropy (e.g. Cu) [10]. In addition, many binders and supporting materials are often required to avoid the aggregation of nanosheets during the fabrication of electrode [11]. However, the poor electronic conductivity of these additives and supporting materials result in a low current density for CO₂ reduction reaction (CO₂RR) process. For example, although ultrathin Cu nanosheet supported onto Ni(OH)₂

* Corresponding authors.

E-mail addresses: phs0727@skku.edu (H.S. Park), byxia@hust.edu.cn (B. Yu Xia).

nanosheets displayed a much higher CO selectivity of CO₂RR compared to the bulk counterpart, the current density was as low as 4.3 mA cm⁻² [12].

In order to resolve this problem, building integrated electrode with hierarchical architecture using the 2D nanomaterials as the building blocks is considered an innovative and feasible strategy. The body-hugging connection of nanosheets in different dimensions facilitates the charge/mass transport, providing abundant active sites exposed on the sheet surface for CO₂RR process [13]. In line with this, we report the synthesis of hierarchically structured electrode composed of ultrathin Cu nanosheets (NS) through a facile galvanic replacement method [14]. These hierarchical NS could be stable in the air for more than four months. Using the integrated Cu electrode for CO₂RR, a high selectivity and activity for CO formation with Faradaic efficiency of 74.1%, partial current density over 23.0 mA cm⁻², and turnover frequency of 0.092 s⁻¹ are achieved. Density functional theory (DFT) calculation demonstrates that the large amount of lattice vacancy defects in the ultrathin porous NS promote the CO formation. This work provides a simple strategy to prepare Cu NS structures and offers new clues to design ultrathin 2D NS for CO₂ electrocatalysts with high selectivity and efficiency.

2. Experimental section

2.1. Preparation of hierarchical Cu nanostructures

In the synthesis for Cu-100-8 integrated electrode, Zn foil was successively cleaned by acetone, deionized water and ethanol. Then, 100 mM CuSO₄ aqueous solution was prepared. The product was made by immersing Zn foil into the CuSO₄ solution for 8 min and washed by deionized water and ethanol. The preparation process of Cu-600-8 was similar with that of Cu-100-8 but the CuSO₄ solution was 600 mM. The experiments with different reaction time of 2, 4, 6 and 10 min were also executed for both 100 mM (Cu-100-2, Cu-100-4, Cu-100-6 and Cu-100-10) and 600 mM CuSO₄ solution. Furthermore, adjusting CuSO₄ concentration of 50, 150, 200, 300, 400, and 500 mM was carried out with the reaction time of 8 min for Cu-50-8, Cu-150-8, Cu-200-8, Cu-300-8, Cu-400-8, and Cu-500-8, respectively. These Cu deposited Zn foils were directly used as working electrodes for the electrochemical measurements.

To investigate the basic properties of Cu nanostructures and compare the performance of integrated electrodes and traditional electrodes, the powder samples of Cu-100-8-P and Cu-600-8-P were prepared by scraping from the surface of Cu-100-8 and Cu-600-8 electrodes, respectively. For testing the electrochemical performance and CO₂RR properties of the powder samples, the working electrodes were fabricated by using the traditional way. The catalysts ink was made by dispersing powder (3 mg) in the mixture solution of water (500 μ L), ethanol (500 μ L) and Nafion solution (25 μ L) by sonicating for 40 min. Then the working electrodes were fabricated by dropping this dispersion (15 μ L) onto a pre-polished glassy carbon electrode.

2.2. Characterizations

X-ray diffraction (XRD) characterization of the powder samples was carried out by employing an x'pert3 powder device (PANalytical B.V.) with Cu target ($\lambda = 1.54056 \text{ \AA}$). X-ray photoelectron spectra (XPS) data were acquired on a Kratos Axis Ultra DLD-600W with incident radiation of monochromatic Al K α x-rays. Scanning electron microscopy (SEM) and Transmission electron microscopy (TEM) investigation was taken with an accelerating voltage of 200 kV. SEM sample was directly cut from the electrodes, while TEM sample was prepared by dispersing the corresponding powder samples (Cu-100-8-P and Cu-600-8-P) into ethanol and dropped on a Cu grid. Atomic force microscopy (AFM) sample was prepared by ultrasonication the mix solution for 1 h and dropped on a silicon wafer. The Brunauer-Emmett-Teller specific surface area was determined by the nitrogen adsorption method using

Micromeritics ASAP 2020 apparatus. The adsorption temperature was 77 K. The pore-size distribution derived from desorption isotherm was analyzed by Barret-Joyner-Halender (BJH) method (cylindrical pore model). The Cu dispersion was evaluated on a basis of the dissociative N₂O adsorption method [15]. To completely oxidize Cu nanostructures, the powder samples were pretreated in air at the flow rate of 30 mL min⁻¹ at 350 °C for 60 min [16]. Then, they were purged with N₂ flow at the rate of 30 mL min⁻¹ for 40 min to remove all the residual O₂. After cooling them to room temperature, temperature-programmed reduction (TPR) measurement was performed by heating the samples to 350 °C at 10 °C min⁻¹ in 10% H₂/N₂ flow (at the flow rate of 30 mL min⁻¹). The reduction reaction of CuO + H₂ \rightarrow Cu + H₂O occurs and causes hydrogen consumption (denoted as X). After the first reduction, the sample was cooled to 50 °C. Then, the surface oxidation of the samples was carried out in N₂O/N₂ atmosphere (at the flow rate of 30 mL min⁻¹) at 50 °C for 30 min. The reaction indicates 2Cu + N₂O \rightarrow Cu₂O + N₂. After this surface oxidation, the samples were subjected to N₂ flow again to remove the oxidant and cooled to room temperature before the second TPR test. The second TPR followed the same procedure as the first TPR procedure, and the reaction undergoes Cu₂O + H₂ \rightarrow 2Cu + H₂O. The hydrogen consumption during the second TPR was denoted as Y. On a basis of these results, the dispersion of Cu (D), specific Cu surface area (S), and average volume-surface diameter (d_{V,S}) were calculated by the equations: D = (2 \times Y/X) \times 100%, S = 2 \times Y \times N_{av}/(X \times M_{Cu} \times 1.4 \times 10¹⁹) \approx 1353 \times Y/X (m² Cu/g Cu), and d_{V,S} = 6/(S \times ρ _{Cu}) \approx 0.5 \times X/Y (nm), respectively [17]. Where N_{av} is the Avogadro's constant (6.02 \times 10²³ mol⁻¹), M_{Cu} is the relative atomic mass (63.5 g mol⁻¹), and ρ _{Cu} is the density of Cu (8.92 g cm⁻³).

2.3. Electrochemical measurements

All the electrochemical properties of the samples were recorded by AutoLab 302 N electrochemical workstation in an H-type electrolyzer. The anode and cathode compartments of electrolyzer were separated by Nafion membrane. The active area of integrated electrodes were controlled as 1 \times 1 cm². The reference electrode and counter electrode was Ag/AgCl and Pt mesh (1 \times 1 cm²), respectively. The electrolyte was 0.5 M KHCO₃ aqueous solution. During the electrochemical tests, the working compartment of the H-type electrolyzer contained 10 mL electrolyte with a gas headspace of 10 mL. Electrode potentials were converted to the reversible hydrogen electrode (RHE) reference scale using E_{Vs. RHE} = E vs. Ag/AgCl + 0.210 V + 0.059 \times pH [6]. All the potentials refer to a reversible hydrogen electrode (RHE). CO₂ was purged into the electrolyte before (30 min) and during the CO₂RR tests to make CO₂-saturated situation. The gas flow rate was 20 mL min⁻¹. The pH of CO₂-saturated 0.5 M KHCO₃ aqueous solution was 7.4. Linear sweep voltammetry (LSV) curves were measured at a scan rate of 10 mV s⁻¹. The onset potential was acquired from the corresponding LSV result to achieve the current density of 1 mA cm⁻². The long-term electrolysis was recorded by the chronoamperometry (GA) test. The cyclic voltammetry (CV) curves were collected by changing the scan rate from 10 to 100 mV s⁻¹. The roughness factor (R_f) for Cu foil was defined to be 1. The electrical impedance spectroscopy (EIS) was tested under the frequencies from 100 kHz to 100 mHz, with the amplitude of 5 mV and applied potential of -0.6 V vs RHE for both integrated electrodes and traditional electrodes made by the powders. To get the Faradaic efficiency of different products, the gas product was guided to a gas chromatograph (GC-2014, Shimadzu) equipped with PLOT Mol Sieve 5A and Q-bond PLOT columns. The gas product was detected via thermal conductivity detector (TCD) for H₂ and flame ionization detector (FID) for CO. The electrochemical reduction measurements were also repeatedly investigated by another online GC system, Panna GC (A-91). The liquid products were analyzed by a ¹H Nuclear Magnetic Resonance (NMR) spectroscopy (Bruker AV400 NMR). The turnover frequencies (TOFs) of Cu for CO formation (TOF_{CO}) were calculated

following the equation: $TOF_{CO} = \frac{j_{CO} * S}{2n_{Cu} F}$. Where j_{CO} is the partial current densities for CO formation at the potential of -1.0 V vs RHE, S is the practical geometric surface area of the integrated electrode (1 cm^2), 2 is derived from the two transferred electrons for CO production, F stands for Faraday constant (96485.3 C/mol), and n_{Cu} indicates the moles number of Cu atoms on the electrode according to the Cu loading [18]. To obtain the value of n_{Cu} for the integrated electrodes, it was assumed that all of the Cu atoms on the electrodes were able to catalyze the CO_2 reduction reaction [19]. Considering that the Cu nanostructures were constructed through the reaction: $\text{Zn}_{(s)}^0 + \text{Cu}_{(aq)}^{2+} \rightarrow \text{Cu}_{(s)}^0 + \text{Zn}_{(aq)}^{2+}$, n_{Cu} was obtained from the mass difference of the Zn foil before and after the reaction as well as the atomic mass difference of Cu and Zn.

2.4. Computational method

All the density functional theory (DFT) calculations were performed using Vienna Ab-initio Simulation Package (VASP) [20,21], taking advantage of the Projected Augmented Wave (PAW) method [22]. The revised Perdew-Burke-Ernzerhof (RPBE) functional was used to describe the exchange and correlation effects [23–25]. For all the geometry optimizations, the cutoff energy was set to be 500 eV. Reciprocally proportional to the surface parameters, a $3 \times 3 \times 1$ Monkhorst-Pack grids [26] was used to carry out all the surface calculations. At least 15 Å vacuum layer was applied in z-direction of the slab models, preventing the vertical interactions between slabs.

The computational hydrogen electrode (CHE) model [27,28] proposed by Norskov et al. was used to calculate the free energies of CO_2 reduction intermediates, based on which the free energy of an adsorbed species was defined as

$$\Delta G_{ads} = \Delta E_{ads} + \Delta E_{ZPE} - T\Delta S_{ads} + \int C_p dT$$

where ΔE_{ads} is the electronic adsorption energy, ΔE_{ZPE} is the zero-point energy difference between adsorbed and gaseous species, $T\Delta S_{ads}$ is the corresponding entropy difference between these two states, and $\int C_p dT$ is the enthalpy correction. The electronic binding energy was referenced as graphene for each C atom, $\frac{1}{2}$ H_2 for each H atom, and $(\text{H}_2\text{O} - \text{H}_2)$ for each O atom, plus the energy of the clean slab.

3. Result and discussion

3.1. Structural and composition analysis

The schematic fabrication process is illustrated in Fig. 1, where a zinc foil is immersed into the aqueous copper sulfate (CuSO_4) solution. Considering the higher standard reduction potential of Cu^{2+}/Cu pair (+0.34 V) than that of Zn^{2+}/Zn pair (-0.76 V), Cu^{2+} ions can be spontaneously reduced by metallic zinc and deposited on the surface of Zn foil [29]. X-ray diffraction (XRD) pattern (Fig. 2a) indicates the face-centered cubic (fcc) structure of metallic Cu nature (JCPDS No. 65-9743) in Cu-100-8-P NS. Compared to the hierarchical Cu-600-8-P NP, Cu-100-8-P NS has a much larger half-peak width, indicating the smaller crystallite size of the latter. As calculated from the Scherrer equation, the grain size of Cu-100-8-P NS is about 3.3 nm, smaller than 28.6 nm of Cu-600-8-P NP. It is worth noting that no obvious oxides peaks of the resulting Cu-100-8-P NS are observed. Generally, additional protectives such as capping agents are required to protect Cu nanostructures from oxidation [30]. On the other hand, this Cu NS is very stable without any protection even for 4 months exposing in the air (Fig. 2b). XPS technique was also employed to further confirm the metallic state of Cu products. The major peak of the initial sample corresponding to $\text{Cu}(2p_{3/2})$ is observed at 932.3 eV, and another peak of $\text{Cu}(2p_{1/2})$ is also present at 952.3 eV (Figure S1). Both peaks suggest that Cu-100-8-P is mainly in the metallic Cu form [12]. For the samples after exposure in the air for 4 months, although a satellite peak for $\text{Cu}(2p_{3/2})$ is appeared at 943.1 eV, this peak is not obvious compared to that of metallic Cu. It should be mentioned that this XPS results can't exclude the adsorbed oxygen and possible formation of copper oxides, as the $\text{Cu}(2p_{3/2})$ peaks for Cu^+ and Cu^0 are overlapped [2]. These findings indicate a phase purity and anti-oxidation of Cu nanostructure despite the exposure in oxygen environment. The atomic force microscope (AFM) results show the irregular NS shape with a thickness of 3–4 nm and a width of micrometer level (Fig. 3). This galvanic replacement method is easy to scale up and be applied for the design of other 2D metal nanosheets.

Field-emission scanning electron microscope (FE-SEM) images of Cu-100-8 demonstrate a hierarchically porous structure assembled by Cu NS (Fig. 4a). The average thickness of these nanosheets is estimated to be sub-10 nm (Fig. 4b). The morphology of the porous NS is further supported by transmission electron microscopy (TEM) images, showing a thickness of 2–4 nm (Fig. 4c). And the size of nanoparticles

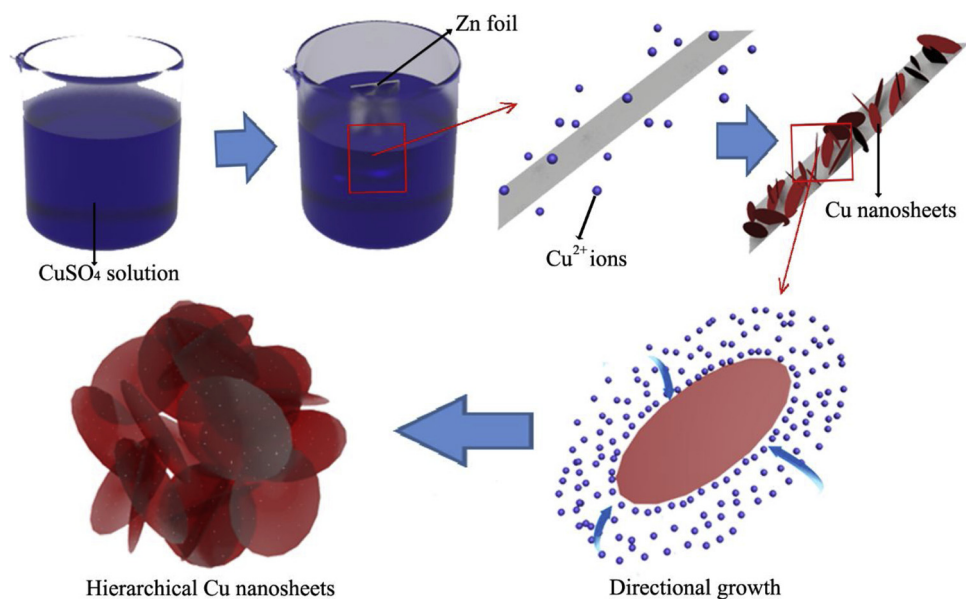


Fig. 1. Synthetic illustration of synthesis procedures and simplified assembly process of Cu NS electrodes.

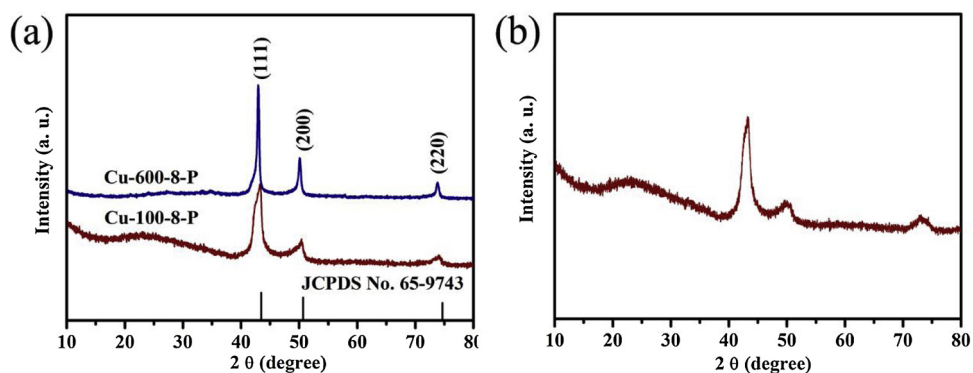


Fig. 2. (a) XRD patterns of Cu-100-8-P NS and Cu-600-8-P NP. (b) XRD curves of the powder scraped from the surface of Cu-100-8 electrode which was placed in the air for 4 months.

corresponding to the size of building unit is about 4 nm. The high-resolution (HR) TEM image (Fig. 4d) reveals the lattice fringe of 0.21 nm, corresponding to the (111) facet of fcc Cu phase [31]. In this study, the growth of Cu nanosheets is dependent on the precursor concentration and reaction time. Experimental results demonstrate that the concentration of Cu ions determines the morphology of the products (Figure S2), while the reaction time affect the width of NS (Figure S3). The anisotropic growth of Cu NS is preferred at a relatively low Cu ion concentration (≤ 200 mM). The concentration-depended morphology can be derived from the different reaction rates and local electric field distribution [32]. At the concentration of 100 mM for Cu ion, a quasi-equilibrium growth of Cu into anisotropic NS is initially carried out due to the sluggish reduction rate (Figure S3a) [33]. Afterwards, a galvanic cell is molded spontaneously and the strong electric field is localized on the edge, thereby providing a driving force for the further growth into a hierarchical Cu NS structure (Fig. 1) [34,35]. At the high concentration of CuSO₄ up to 600 mM, a fast growth rate eliminates the preferential orientation, leading to a relatively isotropic structure of Cu nanoparticles (Cu-600-8) for the construction of a hierarchical architecture in different manners to Cu NS (Figures S4 and S5) [36]. According to the TEM image (Figure S4c), the size of an individual nanoparticle is about 45 nm.

Considering the porous structure is beneficial for the electrochemical reaction happed at the gas-liquid-solid interface, we then employ nitrogen (N₂) adsorption-desorption method to further analyze the porosity of the samples. N₂ adsorption-desorption isotherms of both Cu-100-8-P NS and Cu-600-8-P NP samples present IV-type and

hysteresis loops of H3-type (Figure S6), which indicates the existence of slitlike pores [37]. The specific surface areas and pore volumes of both samples have also been calculated based on these sorption results. Cu-100-8-P NS exhibits a higher BET specific surface area ($24.3 \text{ m}^2 \text{ g}^{-1}$) and larger total pore volume ($0.24 \text{ cm}^3 \text{ g}^{-1}$) than those of Cu-600-8-P NP ($12.6 \text{ m}^2 \text{ g}^{-1}$ and $0.09 \text{ cm}^3 \text{ g}^{-1}$). In addition, the pore-size analysis suggests the presence of mesopores and macropores with a wide distribution from 3 to 200 nm (Figure S6). The existence of macro-/mesopore could ensure the rapid mass transfer and diffusion of electrolyte, which can further enhance the CO₂RR performance.

To better understand the physicochemical properties of the as-prepared Cu nanostructures, the chemisorption of N₂O experiments have been carried out [38]. The reduction profiles of calcined Cu nanostructures are obtained before and after N₂O oxidation at 50 °C (Figure S7). On the basis of hydrogen consumptions during both TPR processes, the dispersion (D), exposed area (S), and average volume-surface diameter (d_{v,s}) of Cu are evaluated for Cu-100-8-P NS and Cu-600-8-P NP nanostructures. Both the Cu dispersion and exposed area of Cu-100-8-P NS are much higher than those of Cu-600-8-P NP (Table S1). Besides, the average volume-surface diameter of Cu-100-8-P NS is 3.8 nm, smaller than 21.1 nm of Cu-600-8-P NP. These values are consistent with the average Cu crystalline size (d_{v,w}) derived from the XRD data and average particle size (d) obtained from TEM images within a marginal range. Given by better Cu dispersion and exposed area, the active sites on Cu-100-8-P NS are more sufficient exposed to reactants, which further improve the CO₂RR catalytic activity [39].

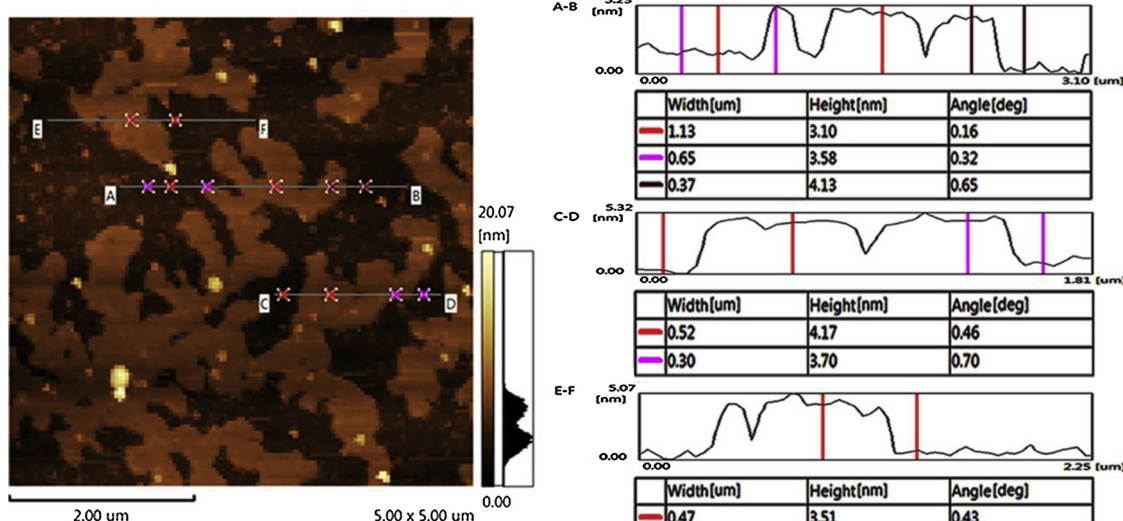


Fig. 3. AFM analysis of Cu-100-8-P NS: the AFM topographical picture (left image) and the corresponding step-height data (right image).

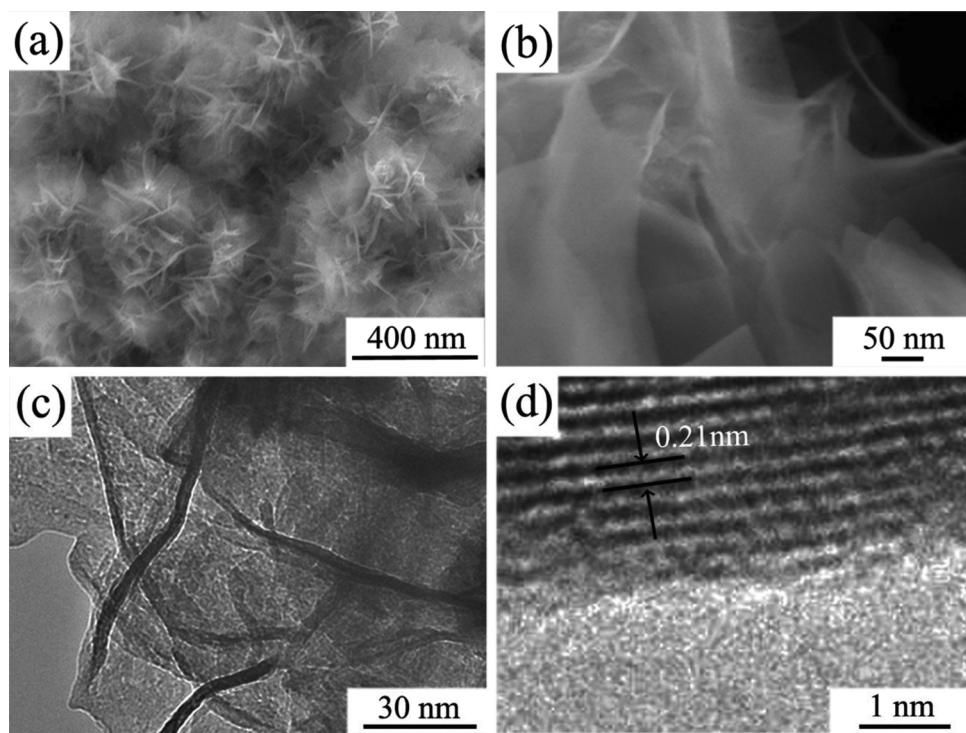


Fig. 4. (a, b) FESEM, (c) TEM, and (d) HRTEM images of Cu-100-8-P.

3.2. CO_2 reduction performance

The self-standing Cu-100-8 electrode is directly employed as the binder-free integrated electrode for CO_2 electroreduction in 0.5 M KHCO_3 aqueous solution. As a comparison to Cu-100-8 NS electrode, the pristine Zn foil substrate and Cu-600-8 NP electrode are used as control samples. As tested in Ar- and CO_2 -saturated 0.5 M KHCO_3 electrolyte, the pristine Zn foil shows relatively small changes of the current densities within the range of applied potentials (Fig. 5a). When the Zn foil is deposited by Cu nanostructures, the electrodes respond violently to CO_2 and exhibit a much higher catalytic current in CO_2 -saturated electrolyte than in Ar condition. Compared with Cu-600-8 NP (-0.35 V), the Cu-100-8 NS electrode achieves a more positive onset potential of -0.29 V and rapidly increasing current density in the more negative potential range. At a potential of -1.1 V, the Cu-100-8 NS electrode displays a total current density of 49.8 mA cm^{-2} , which is almost twice than 26.4 mA cm^{-2} for Cu-600-8 NP electrode and 5.7 times higher than 7.4 mA cm^{-2} for Zn foil, respectively. This onset potential is also more positive than most of the other published Cu-based electrodes [40]. These results strongly support a remarkable CO_2 reduction performance of Cu NS on the surface of Zn foil.

Considering the weak selectivity of Cu-based electrode, the products reduced from CO_2 are analyzed by the stepped electrolysis at each applied potential (Figure S8). Only CO and H_2 are found as the gas product by GC. The liquid products are also tested by ^1H NMR spectroscopy. Only trace amounts of formic acid (HCOOH) are detected, as shown in the NMR result of product produced at -1.0 V (Figure S9). Besides, the total FE for CO and H_2 production is almost 100% in all the potential range. Therefore, the FE of liquid products could be negligible. Although Cu-based CO_2 RR electrodes are famous for its polycarbon compounds production, the products of CO_2 RR on these Cu-based integrated electrodes are only CO and H_2 . The Faradaic efficiencies for CO (FE_{CO}) and H_2 (FE_{H_2}) are estimated as shown in Fig. 5b and Figure S10, respectively, while the partial current densities for CO (j_{CO}) and H_2 (j_{H_2}) at the specified potential are measured to evaluate their formation efficiencies (Figure S11). Obviously, Cu-100-8 NS electrode presents a larger value of both FE_{CO} and j_{CO} as well as a lower

FE_{H_2} compared to those of Zn foil and Cu-600-8 NP electrodes at all the applied potentials. All the Cu NS synthesized at different reaction times and Cu ion concentrations show a much higher CO_2 RR performance than other nanostructures, such as nanofoam and nanoparticles (Figures S12-S14). Moreover, the turnover frequency (TOF) values of Cu electrodes for CO formation (TOF_{CO}) are calculated to further evaluate the catalytic activity. Among all Cu-based samples, the Cu-100-8 NS electrode exhibits the best CO_2 RR performance to CO formation (Table S2). The maximum FE_{CO} of Cu-100-8 NS electrode is 74.1% at potential of -1.0 V vs RHE, which is about 1.6 times of 45.2% for Cu-600-8 NP electrode and 2.6 times of 28.5% for Zn foil. At the same time, the FE_{H_2} of Cu-100-8 NS is 24.8% at this potential, which is much lower than those of Cu-600-8 NP (54.4%) and Zn foil (69.9%). The j_{CO} of Cu-100-8 NS electrode is 23.0 mA cm^{-2} , higher than 8.3 mA cm^{-2} for Cu-600-8 NP electrode and 1.1 mA cm^{-2} for Zn foil. The TOF_{CO} of Cu-100-8 NS electrode is 0.092 s^{-1} at -1.0 V vs RHE, which is much higher than 0.008 s^{-1} of Cu-600-8 NP electrode, indicating the outstanding catalytic activity of the former for CO_2 conversion into CO. In comparison to other previous Cu-based electrocatalysts reported for CO_2 RR, our Cu NS electrode achieves larger FE_{CO} , partial CO current density, and TOF for CO formation (Table S3). In particular, the “brick-and-mortar” Cu-100-8-P NS and Cu-600-8 NP electrodes fabricated by the traditional electrode fabrication method show similar FEs but much smaller current densities than binder-free integrated electrode (Fig. 5c). This binder-free integrated electrode greatly enhance the efficiency of CO_2 conversion without significantly sacrificing the product selectivity (Figure S15). Moreover, the CO_2 RR performance of Cu-100-8 NS and 600-8 NP electrodes remain stable during a long-term electrolysis of 20 h (Fig. 5d and Figure S16). The total current density, FE_{CO} and FE_{H_2} are almost settled in about 31 mA cm^{-2} , 74% and 25%, respectively. Although the CO_2 RR performance of the integrated electrodes didn't be tested after 20 h, it shows excellent catalytic stability during the 20 h electrolysis. Furthermore, the crystalline phase, crystallinity, as well as the structures stabilities of both samples for the 20 h electrolysis have been investigated. As shown by the XRD patterns (Figure S17), the Cu-100-8 and Cu-600-8 after long-term electrolysis almost keep the same crystalline phase and crystallinity as just prepared. SEM images also suggest

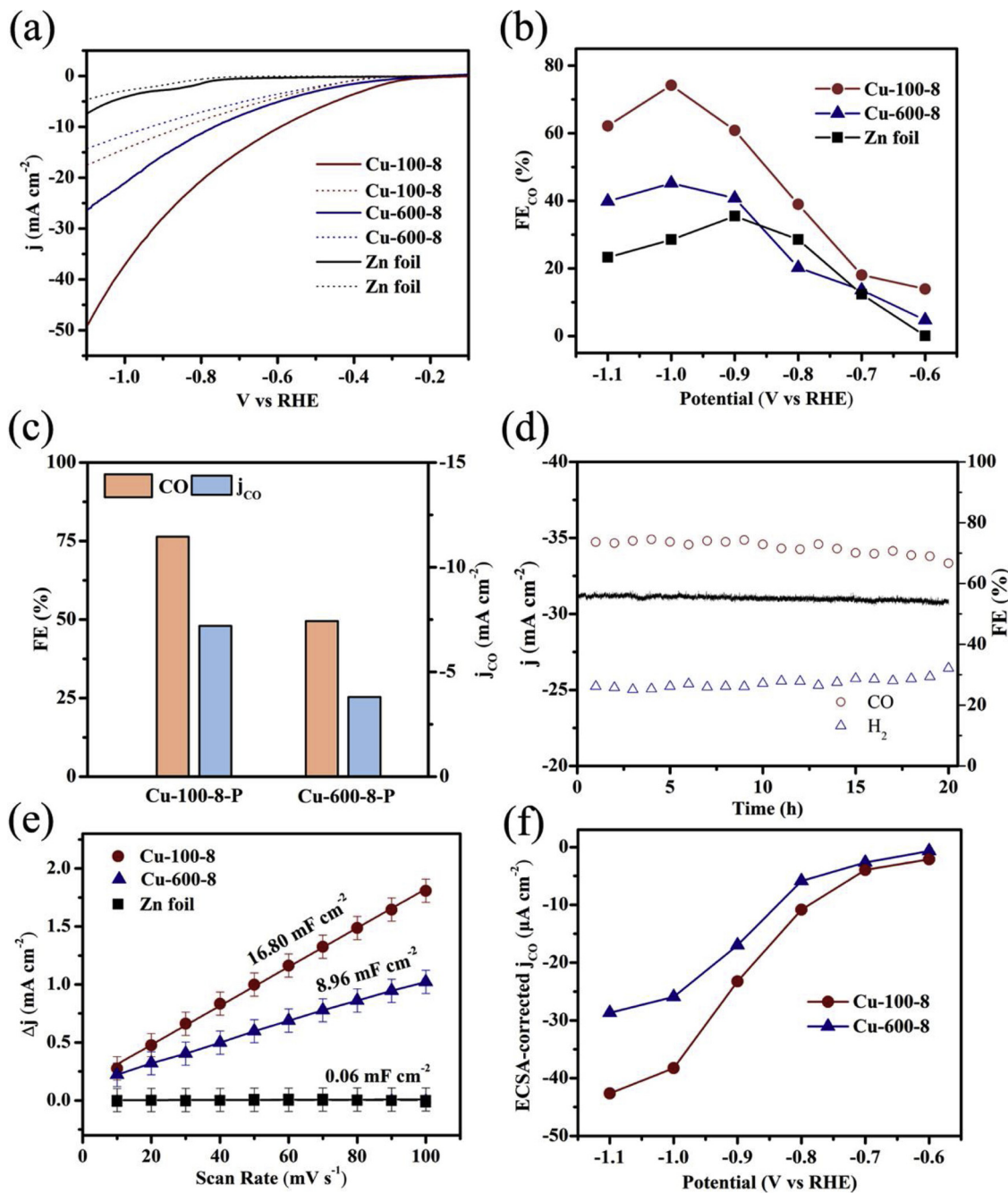


Fig. 5. (a) Polarization curves of the integrated electrodes in the Ar- (dashed line) or CO₂-saturated (solid line) 0.5 M KHCO₃ electrolyte; (b) FEs of CO at various applied potentials for the integrated electrodes; (c) FEs and partial current density of CO at -1.0 V for traditional electrodes made by Cu-100-8-P and Cu-600-8-P; (d) Long-term electrolysis of Cu-100-8 electrode at -1.0 V; (e) Current density differences against scan rates at 0.5 V, and (f) ECSA-corrected CO current densities of Cu-100-8 NS and-600-8 Cu NP electrodes.

their good structure stability (Figure S18). These results confirm an excellent durability of the Cu-100-8 electrodes for a long-term electrolysis compared with other published Cu-based electrodes (Fig. 5d and Table S3).

3.3. Enhanced CO₂ reduction activity over Cu NS electrode

The catalytic activity of active material is known to be determined by the extrinsic charge and mass transport of the electrode, as well as the intrinsic and apparent activities [41]. To find the reason for higher catalytic activity of porous Cu NS, several electrochemical analyses are performed. Nyquist plots of the electrodes are firstly measured to investigate equivalent series (ESR) and charge transfer resistances (R_{ct})

during the CO₂RR process (Figure S19). The charge transfer resistances (R_{ct}) of Cu-100-8 NS electrode, Cu-600-8 NP electrode, and pristine Zn foil are 4.2, 7.4, and 15.3 Ω, respectively. Moreover, Cu-100-8 NS electrode shows the lowest ESR value. No ancillary materials are included in the binder-free integrated electrode, which is associated with the lower impedance than the traditional “brick-and-mortar” electrode [42]. Nyquist plots of the traditional electrodes fabricated by the corresponding powder samples are tested to investigate the advantages of integrated electrodes (Figure S20). The electrodes made by Cu-100-8-P NS and Cu-600-8-P NP powders exhibit much larger R_{ct} of 268.7 and 375.0 Ω than that of the corresponding integrated electrodes, respectively. The low ESR and R_{ct} of the integrated Cu-100-8 NS electrode are attributed to the higher electronic conductivity of Cu than Zn and the

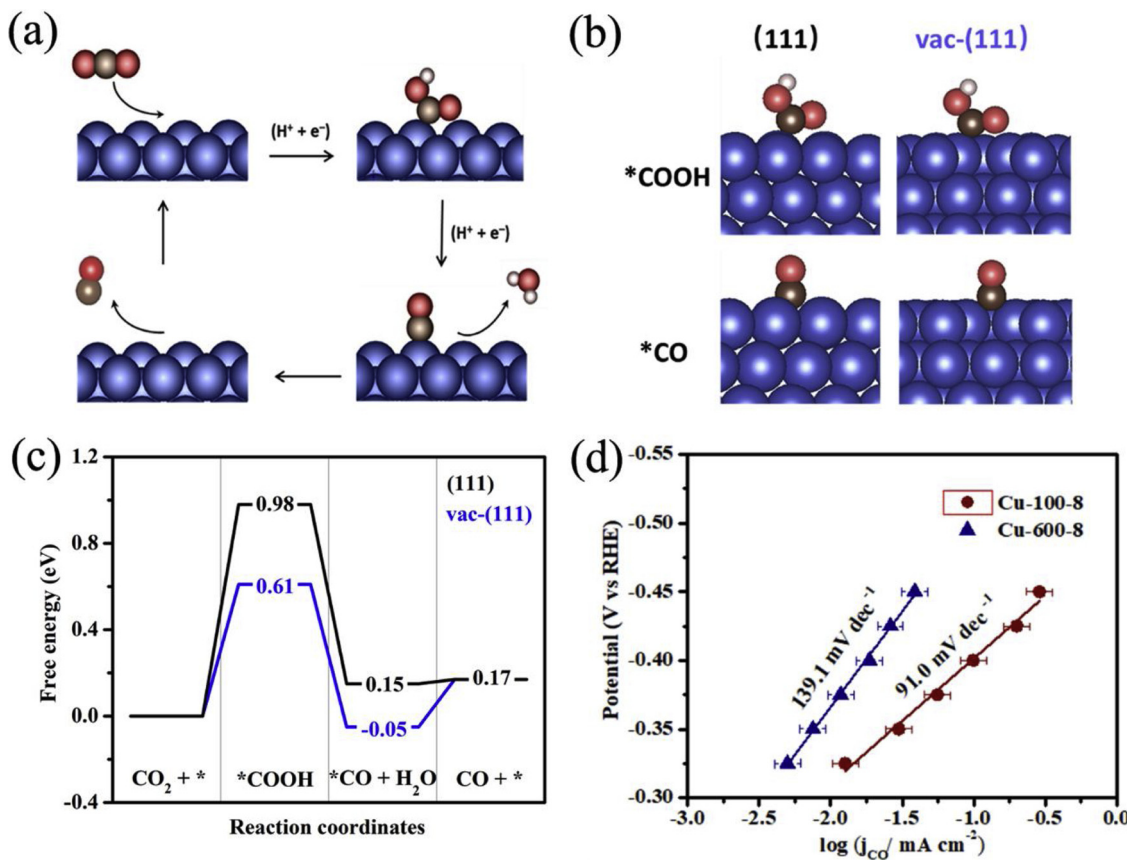


Fig. 6. (a) Schematic illustration of CO₂ reduction to CO via a two-electron transfer mechanism; (b) Side view of the binding configurations of *COOH and *CO on the Cu (111) and vac-(111) surfaces; (c) CO₂ reduction reaction coordinates on the Cu (111) and vac-(111) surfaces; (d) Tafel plots of CO production for Cu-100-8 NS and Cu-600-8 NP electrodes.

fast charge transport through 2D anisotropic pathways [43]. Besides, the body-hugging contact of Cu NS derived from the hierarchical construction further enhances the electronic transportation at the surface/interface of the integrated electrode [44].

Considering the abundant vacancies defects and atoms exposed on surface, as well as the good Cu dispersion and large accessible surface area, porous Cu ultrathin NS are predicted to achieve plentiful and highly active sites. To authenticate the prediction, the electrochemically active surface area (ECSA) of the electrodes in a close correlation with the active sites are also investigated. In view of the proportion of the double layer capacitance (C_{dl}) to ECSA, the value of C_{dl} is estimated varying the scan rates of CV (Figure S21). As shown in Fig. 5e, the values of C_{dl} are 16.80 and 8.96 mF cm⁻² for Cu-100-8 NS electrode and Cu-600-8 NP electrode, respectively (Table S4). Relatively, the specific capacitance (Cs) for a rather flat Cu surface, which has the equal value of the geometric area and active area, is 28 μF cm⁻² [45]. On basis of the defined surface roughness factor (~1) for this flat Cu foil, the ECSAs are estimated as 600 and 320 cm² for Cu-100-8 NS and Cu-600-8 NP electrodes, respectively. These results confirm the dramatically enhanced ECSA and the large number of activity sites for the hierarchically structured porous NS. Furthermore, the ECSA-corrected partial current densities for CO supports the better intrinsic activity of Cu-100-8 NS electrode than that of Cu-600-8 NP for CO₂RR (Fig. 5f) [46]. Furthermore, the values of C_{dl}, ECSAs and ECSA-corrected j_{CO} at various applied potential are tested and calculated for other Cu-based electrodes (Table S4-5 and Figure S22). Although some non-nanosheets electrodes exhibit larger C_{dl} and ECSAs than some nanosheets electrodes. However, all the nanosheets electrodes show higher ECSA-corrected j_{CO} than other kinds of nanostructures electrodes, especially at relatively more negative potential (-0.8 ~1.1 V).

These results further confirm the better intrinsic activities of CO formation for the Cu NS electrodes.

3.4. Defect effect for the intrinsic activity of Cu NS electrode

As shown in the above CO₂RR results, Cu NS electrodes exhibit improved CO production than other Cu nanostructures. This phenomenon is in accordance with recent publication of Cu NS structure [12]. Given by the surface-dominated reactions occurring on Cu NS for CO₂RR, the surface defects are supposed to be one factor for the enhanced intrinsic activity of Cu NS [47]. DFT calculations are performed to understand the contribution of the smooth Cu(111) surface and vacancy-contained Cu(111) surface (vac-Cu(111)) to the CO₂RR. Typically, although two electrons for each CO₂ are transferred in the whole reaction, the reduction of CO₂ to produce CO in aqueous condition occurs in the following three elementary steps (Fig. 6a) [48–50]: (1) CO₂ + (H⁺ + e⁻) + * → *COOH, (2) *COOH + (H⁺ + e⁻) → *CO + H₂O, and (3) *CO → CO↑ + * step, where * denotes the active sites on the catalyst surface. The corrections of zero-point energy, entropy, and enthalpy of adsorbed and gaseous species can be found in Table S6. Based on the afore-mentioned reaction pathway, the free energies of two intermediate states such as *COOH and *CO are the key parameters to determine the catalytic activity (Fig. 6b). Employing the computational hydrogen electrode (CHE) model, the free energies on Cu(111) and vac-(111) surfaces are estimated as shown in Fig. 6c. Considering the higher free energy than other steps, the first step (* + (H⁺ + e⁻) + CO₂ → *COOH) is regarded as the rate-determining step for both surfaces. The free energy change (ΔG) of this step on Cu(111) is 0.98 eV, indicating a slow initial kinetics and thus a high potential required to initiate the reaction. Comparatively, the free energy change (ΔG) of

vac-Cu(111) for this elementary step was sharply dropped to 0.61 eV, suggesting an accelerated initial kinetics and thus improved reaction performance.

To further verify this hypothesis, Tafel plots of CO production for these electrodes are analyzed. All the Cu NS electrodes exhibit Tafel slopes in the range of 88.6–93.9 mV dec⁻¹, which is smaller than those of other Cu nanostructures (Figures S23 and S24). The Tafel slopes of Cu-100-8 NS and Cu-600-8 NP electrodes are 91.0 and 139.1 mV dec⁻¹, respectively (Fig. 6d). Both slopes are in accordance with an initial rate-determining 1e- transfer mechanism as demonstrated by DFT calculations [51]. At the same time, a relatively smaller Tafel slope of Cu NS indicates a faster 1e- pre-equilibrium transfer. In this regard, the optimized free energy pathway of the first electron transfer step is associated with the increased number of vacancies defects, resulting in a high intrinsic catalytic activity of the hierarchically structured Cu NS.

4. Conclusion

In summary, the hierarchically structured porous Cu NS integrated electrode is successfully synthesized through a facile galvanic replacement approach. This synthesis of integrated electrode can simplify the catalyst preparation and integrated electrode fabrication for high performance electrocatalysis applications. Employing the optimized Cu NS electrode, a remarkable CO₂RR activity for converting CO₂ into CO with FE_{CO} of 74.1%, j_{CO} of 23.0 mA cm⁻² and TOF_{CO} of 0.092 s⁻¹ is achieved. The significant CO₂RR performance is attributed to the rapid mass and electrons transport as well as abundant active sites and associated intrinsic activity, which are related to the ultrathin thickness, porous structure, hierarchical construction of the binder-free Cu NS electrode. The DFT calculations confirm that the plentiful lattice vacancies on Cu (111) are responsible for the enhanced intrinsic activity for CO formation. This finding is supported by the lower ESR and R_{CT}, larger ESCA, and smaller Tafel slope of NS than other nanostructures. Therefore, this work provides a design guideline to prepare the integrated electrocatalytic electrodes based on 2D metal nanosheets for CO₂RR, as well as the fundamental understanding about the relation between the structure and electrocatalytic activity for efficient electrochemical conversion of CO₂.

Acknowledgement

This work is financially supported by National 1000 Young Talents Program of China. The Fundamental Research Funds for the Central Universities (2018KFYXKJC044, 2018KFYXJJ121, 2017KFXKJC002, 2017KFYXJJ164) and the Innovation Foundation of Shenzhen Government (JCYJ20160408173202143) are also acknowledged. H. S. Park acknowledges financial support from the National Research Foundation (NRF) funded by the Ministry of Science, ICT & Future Planning of the Korean Government (NRF-2015R1A1A1A05027727). The authors also acknowledge the support of the Analytical and Testing Center of Huazhong University of Science and Technology for XRD, SEM, TEM and AFM measurements.

Appendix A. Supplementary data

Supplementary material related to this article can be found, in the online version, at doi:<https://doi.org/10.1016/j.apcatb.2019.05.038>.

References

- [1] J.T. Billy, A.C. Co, Reducing the onset potential of CO₂ electroreduction on CuRu bimetallic particles, *Appl. Catal. B: Environ.* 237 (2018) 911–918.
- [2] J. Zeng, K. Bejtka, W. Ju, M. Castellino, A. Chiodoni, A. Sacco, M.A. Parkhondel, S. Hernández, D. Rentsch, C. Battaglia, Advanced Cu-Sn foam for selectively converting CO₂ to CO in aqueous solution, *Appl. Catal. B: Environ.* 236 (2018) 475–482.
- [3] A. Aljabor, H. Coskun, D.H. Apaydin, F. Ozel, A.W. Hassel, P. Stadler, N.S. Sariciftci, M. Kus, Nanofibrous cobalt oxide for electrocatalysis of CO₂ reduction to carbon monoxide and formate in an acetonitrile-water electrolyte solution, *Appl. Catal. B: Environ.* 229 (2018) 163–170.
- [4] C. Li, H. Liu, Z. Yu, Novel and multifunctional inorganic mixing salt-templated 2D ultrathin Fe/Co-N/S-carbon nanosheets as effectively bifunctional electrocatalysts for Zn-air batteries, *Appl. Catal. B: Environ.* 241 (2019) 95–103.
- [5] Y. Liu, H. Zhang, J. Ke, J. Zhang, W. Tian, X. Xu, X. Duan, H. Sun, M.O. Tade, S. Wang, OD (Mo₂)/2D (g-C₃N₄) heterojunctions in Z-scheme for enhanced photocatalytic and electrochemical hydrogen evolution, *Appl. Catal. B: Environ.* 228 (2018) 64–74.
- [6] F. Li, M. Xue, J. Li, X. Ma, L. Chen, X. Zhang, D.R. MacFarlane, J. Zhang, Unlocking the electrocatalytic activity of antimony for CO₂ reduction by two-dimensional engineering of the bulk material, *Angew. Chem. Int. Edit.* 129 (2017) 14910–14914.
- [7] S. Gao, Y. Lin, X. Jiao, Y. Sun, Q. Luo, W. Zhang, D. Li, J. Yang, Y. Xie, Partially oxidized atomic cobalt layers for carbon dioxide electroreduction to liquid fuel, *Nature* 529 (2016) 68.
- [8] F. Lei, W. Liu, Y. Sun, J. Xu, K. Liu, L. Liang, T. Yao, B. Pan, S. Wei, Y. Xie, Metallic tin quantum sheets confined in graphene toward high-efficiency carbon dioxide electroreduction, *Nat. Commun.* 7 (2016) 12697.
- [9] K. Xu, P. Chen, X. Li, Y. Tong, H. Ding, X. Wu, W. Chu, Z. Peng, C. Wu, Y. Xie, Metallic nickel nitride nanosheets realizing enhanced electrochemical water oxidation, *J. Am. Chem. Soc.* 137 (2015) 4119–4125.
- [10] X.P. Zhang, J. Han, J.J. Plombon, A.P. Sutton, D.J. Srolovitz, J.J. Boland, Nanocrystalline copper films are never flat, *Science* 357 (2017) 397–399.
- [11] W. Wan, X. Liu, H. Li, X. Peng, D. Xi, J. Luo, 3D carbon framework-supported CoNi nanoparticles as bifunctional oxygen electrocatalyst for rechargeable Zn-air batteries, *Appl. Catal. B: Environ.* 240 (2019) 193–200.
- [12] L. Dai, Q. Qin, P. Wang, X. Zhao, C. Hu, P. Liu, R. Qin, M. Chen, D. Ou, C. Xu, Ultrastable atomic copper nanosheets for selective electrochemical reduction of carbon dioxide, *Sci. Adv.* 3 (2017) 1701069.
- [13] J. Liu, Y. Liu, D. Xu, Y. Zhu, W. Peng, Y. Li, F. Zhang, X. Fan, Hierarchical “nanoroll” like Mo₂/Ti₃C₂T_x hybrid with high electrocatalytic hydrogen evolution activity, *Appl. Catal. B: Environ.* 241 (2019) 89–94.
- [14] J.-S. Jang, W.-T. Koo, S.-J. Choi, I.-D. Kim, Metal organic framework-templated chemiresistor: sensing type transition from P-to-N using hollow metal oxide polyhedron via galvanic replacement, *J. Am. Chem. Soc.* 139 (2017) 11868–11876.
- [15] L.-C. Chen, S.D. Lin, The ethanol steam reforming over Cu-Ni/SiO₂ catalysts: effect of Cu/Ni ratio, *Appl. Catal. B: Environ.* 106 (2011) 639–649.
- [16] R. Chimentao, F. Medina, J. Fierro, J. Llorca, J. Sueras, Y. Cesteros, P. Salagre, Propene epoxidation by nitrous oxide over Au-Cu/TiO₂ alloy catalysts, *J. Mol. Catal. A Chem.* 274 (2007) 159–168.
- [17] C. Van Der Grift, A. Wielers, B. Jogh, J. Van Beunum, M. De Boer, M. Versluijs-Helder, J. Geus, Effect of the reduction treatment on the structure and reactivity of silica-supported copper particles, *J. Catal.* 131 (1991) 178–189.
- [18] D. Gao, H. Zhou, J. Wang, S. Miao, F. Yang, G. Wang, J. Wang, X. Bao, Size-dependent electrocatalytic reduction of CO₂ over Pd nanoparticles, *J. Am. Chem. Soc.* 137 (2015) 4288–4291.
- [19] M. Miao, R. Hou, Z. Liang, R. Qi, T. He, Y. Yan, K. Qi, H. Liu, G. Feng, B.Y. Xia, Chainmail catalyst of ultrathin P-doped carbon shell-encapsulated nickel phosphides on graphene towards robust and efficient hydrogen generation, *J. Mater. Chem. A* 6 (2018) 24107–24113.
- [20] G. Kresse, J. Hafner, Ab initio molecular-dynamics simulation of the liquid-metal-amorphous-semiconductor transition in germanium, *Phys. Rev. B* 49 (1994) 14251.
- [21] G. Kresse, J. Furthmüller, Efficient iterative schemes for ab initio total-energy calculations using a plane-wave basis set, *Phys. Rev. B* 54 (1996) 11169.
- [22] P.E. Blöchl, Projector augmented-wave method, *Phys. Rev. B* 50 (1994) 17953.
- [23] J.P. Perdew, K. Burke, M. Ernzerhof, Generalized gradient approximation made simple, *Phys. Rev. Lett.* 77 (1996) 3865.
- [24] Y. Zhang, W. Yang, Comment on “Generalized gradient approximation made simple”, *Phys. Rev. Lett.* 80 (1998) 890.
- [25] B. Hammer, L.B. Hansen, J.K. Nørskov, Improved adsorption energetics within density-functional theory using revised Perdew-Burke-Ernzerhof functionals, *Phys. Rev. B* 59 (1999) 7413.
- [26] H.J. Monkhorst, J.D. Pack, Special points for Brillouin-zone integrations, *Phys. Rev. B* 13 (1976) 5188.
- [27] A.A. Peterson, F. Abild-Pedersen, F. Studt, J. Rossmeisl, J.K. Nørskov, How copper catalyzes the electroreduction of carbon dioxide into hydrocarbon fuels, *Energy Environ. Sci.* 3 (2010) 1311–1315.
- [28] J.K. Nørskov, J. Rossmeisl, A. Logadottir, L. Lindqvist, J.R. Kitchin, T. Bligaard, H. Jonsson, Origin of the overpotential for oxygen reduction at a fuel-cell cathode, *J. Phys. Chem. B* 108 (2004) 17886–17892.
- [29] S.W. Chee, S.F. Tan, Z. Baraissov, M. Bosman, U. Mirsaidov, Direct observation of the nanoscale Kirkendall effect during galvanic replacement reactions, *Nat. Commun.* 8 (2017) 1224.
- [30] M. Xu, J. Wang, T. Yu, J. Wang, M. Shen, New insight into Cu/SAPO-34 preparation procedure: impact of NH₄-SAPO-34 on the structure and Cu distribution in Cu-SAPO-34 NH₃-SCR catalysts, *Appl. Catal. B: Environ.* 220 (2018) 161–170.
- [31] Z. Meng, S. Cai, R. Wang, H. Tang, S. Song, P. Tsakaros, Bimetallic-organic framework-derived hierarchically porous Co-Zn-N-C as efficient catalyst for acidic oxygen reduction reaction, *Appl. Catal. B: Environ.* 244 (2019) 120–127.
- [32] X. Xia, Y. Wang, A. Ruditskiy, Y. Xia, Galvanic replacement: a simple and versatile route to hollow nanostructures with tunable and well-controlled properties, *Adv. Mater.* 25 (2013) 6313–6333.
- [33] R. Liu, A. Sen, Unified synthetic approach to silver nanostructures by galvanic displacement reaction on copper: from nanobelts to nanoshells, *Chem. Mater.* 24

(2011) 48–54.

[34] X. Lu, H.-Y. Tuan, J. Chen, Z.-Y. Li, B.A. Korgel, Y. Xia, Mechanistic studies on the galvanic replacement reaction between multiply twinned particles of Ag and HAuCl₄ in an organic medium, *J. Am. Chem. Soc.* 129 (2007) 1733–1742.

[35] Z.S. Wu, S. Pei, W. Ren, D. Tang, L. Gao, B. Liu, F. Li, C. Liu, H.M. Cheng, Field emission of single-layer graphene films prepared by electrophoretic deposition, *Adv. Mater.* 21 (2009) 1756–1760.

[36] G. Liu, W. Cai, C. Liang, Trapeziform Ag nanosheet arrays induced by electrochemical deposition on Au-coated substrate, *Cryst. Growth Des.* 8 (2008) 2748–2752.

[37] J. Zhang, J. Yu, Y. Zhang, Q. Li, J.R. Gong, Visible light photocatalytic H₂-production activity of CuS/ZnS porous nanosheets based on photoinduced interfacial charge transfer, *Nano Lett.* 11 (2011) 4774–4779.

[38] Z. Yuan, L. Wang, J. Wang, S. Xia, P. Chen, Z. Hou, X. Zheng, Hydrogenolysis of glycerol over homogeneously dispersed copper on solid base catalysts, *Appl. Catal. B: Environ.* 101 (2011) 431–440.

[39] J. Gong, H. Yue, Y. Zhao, S. Zhao, L. Zhao, J. Lv, S. Wang, X. Ma, Synthesis of ethanol via syngas on Cu/SiO₂ catalysts with balanced Cu⁰-Cu⁺ sites, *J. Am. Chem. Soc.* 134 (2012) 13922–13925.

[40] D. Raciti, K.J. Livi, C. Wang, Highly dense Cu nanowires for low-overpotential CO₂ reduction, *Nano Lett.* 15 (2015) 6829–6835.

[41] J. Pan, X.L. Tian, S. Zaman, Z. Dong, H. Liu, H.S. Park, B.Y. Xia, Recent progress on bifunctional transition metal oxides for Li-air and Zn-air batteries, *Batter. Supercaps* 2 (2019) 336–347.

[42] J. Pan, Y.Y. Xu, H. Yang, Z. Dong, H. Liu, B.Y. Xia, Advanced architectures and relatives of air electrodes in Zn-air batteries, *Adv. Sci.* 5 (2018) 1700691.

[43] L. Lu, Y. Shen, X. Chen, L. Qian, K. Lu, Ultrahigh strength and high electrical conductivity in copper, *Science* 304 (2004) 422–426.

[44] Z. Kou, L. Zhang, Y. Ma, X. Liu, W. Zang, J. Zhang, S. Huang, Y. Du, A.K. Cheetham, J. Wang, 2D carbide nanomeshes and their assembling into 3D microflowers for efficient water splitting, *Appl. Catal. B: Environ.* 243 (2019) 678–685.

[45] P. Waszczuk, P. Zelenay, J. Sobkowiak, Surface interaction of benzoic acid with a copper electrode, *Electrochim. Acta* 40 (1995) 1717–1721.

[46] S. Gao, X. Jiao, Z. Sun, W. Zhang, Y. Sun, C. Wang, Q. Hu, X. Zu, F. Yang, S. Yang, Ultrathin Co₃O₄ layers realizing optimized CO₂ electroreduction to formate, *Angew. Chem. Int. Edit.* 55 (2016) 698–702.

[47] K. Li, R. Zhang, R. Gao, G.-Q. Shen, L. Pan, Y. Yao, K. Yu, X. Zhang, J.-J. Zou, Metal-defected spinel Mn_xCo_{3-x}O₄ with octahedral Mn-enriched surface for highly efficient oxygen reduction reaction, *Appl. Catal. B: Environ.* 244 (2019) 536–545.

[48] W. Zhu, R. Michalsky, Ö. Metin, H. Lv, S. Guo, C.J. Wright, X. Sun, A.A. Peterson, S. Sun, Monodisperse Au nanoparticles for selective electrocatalytic reduction of CO₂ to CO, *J. Am. Chem. Soc.* 135 (2013) 16833–16836.

[49] Q. Li, J. Fu, W. Zhu, Z. Chen, B. Shen, L. Wu, Z. Xi, T. Wang, G. Lu, J.-J. Zhu, Tuning Sn-Catalysis for electrochemical reduction of CO₂ to CO via the Core/Shell Cu/SnO₂ structure, *J. Am. Chem. Soc.* 139 (2017) 4290–4293.

[50] M.B. Ross, C.T. Dinh, Y. Li, D. Kim, P. De Luna, E.H. Sargent, P. Yang, Tunable Cu enrichment enables designer syngas electrosynthesis from CO₂, *J. Am. Chem. Soc.* 139 (2017) 9359–9363.

[51] Y. Chen, M.W. Kanan, Tin oxide dependence of the CO₂ reduction efficiency on tin electrodes and enhanced activity for tin/tin oxide thin-film catalysts, *J. Am. Chem. Soc.* 134 (2012) 1986–1989.